High-resolution, high-transmission soft x-ray spectrometer for the study of biological samples

Authors:

O. Fuchs, L. Weinhardt*, M. Blum, M. Weigand, and E. Umbach
Universität Würzburg, Experimentelle Physik II, Am Hubland, 97074 Würzburg, Germany

M. Bär and C. Heske
Department of Chemistry, University of Nevada, 4505 Maryland Pkwy., Las Vegas, NV 89154-4003, USA

J. Denlinger, Y.-D. Chuang, W. McKinney, and Z. Hussain
Advanced Light Source, Lawrence Berkeley National Laboratory, Berkeley, CA 94720, USA

E. Gullikson, M. Jones, and P. Batson
Center for X-ray Optics, Material Science Division, Lawrence Berkeley National Laboratory, Berkeley, CA 94720, USA

B. Nelles,
Carl Zeiss Laser Optics GmbH, Carl-Zeiss-Str. 22, 73447 Oberkochen, Germany

R. Follath
Berliner Elektronenspeicherring-Gesellschaft für Synchrotronstrahlung m.b.H., Albert-Einstein-Str. 15, 12489 Berlin, Germany

* To whom correspondence should be addressed: lothar.weinhardt@physik.uni-wuerzburg.de (L. Weinhardt), phone: +49 931 31 83570.

Abstract:
We present a variable line-space grating spectrometer for soft x-rays that covers the photon energy range between 130 and 650 eV. The optical design is based on the Hettrick-Underwood principle and tailored to synchrotron-based studies of radiation-sensitive biological samples. The spectrometer is able to record the entire spectral range in one shot, i.e. without any mechanical motion, at a resolving power of 1200 or better. Despite its slit-less design, such a resolving power can be achieved for a source spot as large as (30 × 3000) μm^2, which is important for keeping beam damage effects in radiation-sensitive samples low. The high spectrometer efficiency allows recording comprehensive two-dimensional resonant inelastic soft x-ray scattering (RIXS) maps with good statistics within several minutes. This is exemplarily demonstrated for a RIXS map of highly oriented pyrolytic graphite, which was taken within 10 min.

Keywords:
resonant inelastic soft x-ray scattering, x-ray absorption, x-ray emission, soft x-ray spectroscopy, VLS grating, HOPG

1. Introduction

With the advent of 3rd generation synchrotron radiation sources, x-ray emission spectroscopy (XES) and resonant inelastic x-ray scattering (RIXS) in the soft x-ray regime has become possible within reasonable data acquisition times, ranging from several minutes to a few hours per spectrum. By studying the evolution of an emission spectrum while varying the excitation energy, a detailed insight into the electronic and chemical structure as well as into a multitude of dynamic processes can be gained. Unfortunately, due to the very low fluorescence yield in

the soft x-ray regime, this information is obtained only at the cost of many hours of valuable measuring time at a high-flux beamline of a synchrotron radiation source. Even worse, such long-term high-intensity measurements are only possible for radiation-resistant samples. Especially the investigation of organic molecules or even biological systems is difficult using XES or RIXS under conventional conditions.

The need for long measuring times due to the low fluorescence yield is exacerbated by the moderate detection efficiency of current state-of-the-art spectrometers. Most soft x-ray spectrometers (e.g.[1-5]) are based on a grazing incidence spherical grating Rowland circle design[6]. Novel concepts often make use of variable line-space (VLS) gratings[7-18]. In order to enable XES/RIXS studies of organic and biological samples, we have designed a VLS spectrometer based on the work of Hettrick and Underwood[12-16]. Since organic materials mostly consist of sulfur, carbon, nitrogen, and oxygen atoms, the spectrometer is optimized for the S $L_{2,3}$ (150 eV), C K (280 eV), N K (400 eV), and O K (525 eV) edges. The major design goal was to yield extremely high transmission at sufficient resolving power of $E/\Delta E \geq 1200$ to allow the collection of high-quality spectra with comparably low excitation photon flux densities. The optics were manufactured by *InSync, Inc.* (spherical mirror) and *Carl Zeiss Optronics GmbH* (mechanically ruled plane diffraction grating). The spectrometer mechanics was built by the Center for X-ray Optics (CXRO), Lawrence Berkeley National Laboratory. The optics were tested at beamline 6.3.2 and the assembled instrument at beamline 8.0.2 of the Advanced Light Source (ALS).

2. The optical design

The basic configuration of our spectrometer is shown in Fig. 1. It features a spherical mirror M and a VLS grating G in inner (positive) diffraction order geometry. This combination, albeit for outer order geometry, was originally proposed by Hettrick and Underwood[12-16] and allows the use of the detector D in normal incidence geometry, thereby yielding optimal quantum efficiency of the CCD detector. A variable aperture A can be used to mask the mirror, which reduces imaging aberrations at the cost of vertical acceptance angle. In practice, this aperture is used solely for alignment purposes, since the imaging aberrations are sufficiently small even with open aperture and do not compromise the overall resolving power, as can be seen in Figure 2. In this figure, the three resolution limits (spot size, aberrations, and spatial resolution of the detector) are plotted as a function of photon energy and diffraction order. All important optical design parameters are summarized in Table 1. Details of the early design stages can be found in[19].

As described above, one major goal was to keep the photon flux density low to minimize or avoid beam-induced effects on radiation-sensitive samples. This can be achieved by maximizing the spot size on the sample and minimizing the excitation flux. To be able to use large spot sizes while still maintaining a high energy resolution even without an entrance slit, a low magnification of the source spot in the energy-dispersive direction on the detector is necessary. By using the inner orders of the diffraction grating and by optimizing the design parameters of the spectrometer, a magnification of one has been achieved. This is equal to the case of the conventional Rowland geometry, but the present VLS design offers a significantly improved throughput for the following reasons: The VLS approach cancels the imaging aberrations sufficiently even for the large solid angle collected by the spherical mirror. Further, the detector can be used in normal incidence geometry, which maximizes its detection efficiency. Finally, the use of optimal diffraction orders (see below) for the different photon energies always keeps the blaze angle of the grating close to ideal, leading to maximal throughput for the whole energy range.

The VLS parameters of the grating were selected such that the spherical aberrations introduced by the light-collecting mirror are largely compensated in the desired photon energy range. For only one specific energy and diffraction order it would be possible to modulate the line density such that the imaging aberrations vanish entirely, leading to a stigmatic image in the dispersive direction. Instead of optimizing the VLS parameters in this way for each energy and order separately, which would require the use of several exchangeable gratings and the translation of the detector, we rather decided to employ one grating and no detector movement. This set-up allows for the simultaneous detection of all four core levels and hence photon energy ranges of interest, extending from from 150 to 525 eV, in appropriate diffraction orders: the lower energies in 1st order (S $L_{2,3}$ emission), the intermediate energies in 2nd order (C K emission), and the higher energies in 3rd order (N and O K emission). For higher energy resolution at slightly decreased intensity, even 4th order can be used for O K emission. The simultaneous optimization for different orders allows us to keep the imaging aberrations low for the entire energy range with only one grating, yielding an aberration-limited resolving power of well above 2000 for all four energy ranges simultaneously (shown in Fig. 2 as discussed above). It also moves the emission lines closer together, which allows studying them simultaneously in one detector image, while still avoiding overlapping spectra.

In order to find the optimum VLS parameters which are the best compromise for all four energies in their respective orders, we performed extensive ray tracing calculations. Conventional ray tracing is done in a sequential way by the numerical calculation of single rays as they propagate through the spectrometer. Naturally, these numerical calculations can only be done for one ray, one photon energy, and one diffraction order at a time. In contrast, our approach is to express all relevant quantities of the ray propagation (i.e. the position, incidence angle, and exit angle on all optical elements and the detector) as closed analytical functions of the parameters defining the ray (i.e. photon energy, diffraction order, origin, and emerging direction). The advantage is, that the symbolic partial derivatives of these functions with respect to all parameters to be optimized can be calculated. The knowledge of these derivatives which form the Jacobian matrix allows the simultaneous optimization of all relevant parameters by Newton's method for several photon energies and diffraction orders in one shot. This approach results in a very robust and quickly converging minimization of the combined imaging aberrations even in a high-dimensional parameter space.

For the current instrument, the optimized parameter set included up to four VLS parameters (line density variation up to the quartic term), the detector tilt angle, and the distance between grating and detector. In the process of optimizing these parameters for all four core levels in their respective orders, it became apparent that tilting and shifting the detector out of the zero order focal plane as well as including higher VLS orders than the cubic term does not lead to significantly smaller imaging aberrations. Therefore, in the final design three VLS-parameters were optimized (i.e., up to the cubic term) with the detector plane in the zero order focus and normal incidence geometry. The derived parameters are listed in Table 1.

The VLS grating has been ruled with the ruling engine GTM6. This engine has an interferometric control, which is used to govern the line density variation of the grating. In contrast to the commonly used mechanical ruling under lubricant protection, we applied a ‘dry’ ruling technique without any lubrication during the ruling process. In this way, any molecular contamination is avoided, which is of importance for the ruling of gratings for space and synchrotron radiation.

A diamond tool was used to rule the blaze profiles by plastic deformation in a film of gold which was thermally vapor deposited and optimized for small micro roughness. After the ruling, a final ion beam etching process was applied to transfer the blaze profile completely

into the blank material. This ion beam etching step makes use of the difference in the etching rates between gold and silicon, which differ typically by a factor of 3. So, the master ruling is starting with a larger blaze angle and ends with the specified profile form. The micro roughness is reduced by nearly the same factor. Micro roughness values of < 0.6 nm r.m.s. have been achieved with this technique. Consequently, gratings produced by the ion beam etching technique have an improved stray light compared to those manufactured by the classical technique.

3. Performance

3.1 Efficiency

Due to the entrance slit-less design, all photons within a solid angle of (11.2 × 18.0) mrad^2 emanating from the source enter the spectrometer. While the acceptance angle in dispersive direction (11.2 mrad) is limited by the size of the focusing optics, the non-dispersive direction (18.0 mrad) is merely limited by the size of the detector, since the focusing properties of mirror and grating are negligible in this direction. The included angles of mirror (φ) and grating ($\alpha+\beta$) were chosen to be 172 degrees. With these angles and a nickel coating the reflectivity is above 50% even at the oxygen K edge for each optical element. In order to maximize the grating efficiency, we introduced a blaze angle of 1.8°. Due to the special selection of diffraction orders described in Section 2, the blazing concentrates the reflected intensity for all four interesting energies simultaneously, leading to theoretical grating efficiencies of 18-25 % in the whole energy range at an assumed micro-roughness of 10 Å (see Table 1). It is worth noting that the used diffraction orders are the most intense for the selected energies, not only in theory, but also confirmed by measurements of the grating efficiency.

For example, at the nitrogen K edge, the 3rd order is more intense than the 0th, 1st, 2nd or 4th (and so on) order. Figure 3 compares the theoretical efficiencies of the selected orders with efficiency measurements taken at beamline 6.3.2 of the ALS. The numbers are also given in Table 1. The grating performs slightly better than the theoretical values at the sulfur L and carbon K edge (Fig. 3). This is due to the fact that the actual blaze angle of the grating (1.8°) is slightly larger (steeper) than the design value of 1.79°. This slight mismatch, together with other unavoidable imperfections of the grating (e.g., roughness and surface oxidation of the coating), consequently lead to a reduced measured efficiency (70%) compared to the theoretical value at the nitrogen and oxygen K edge in 3rd order.

The detector is another crucial component for high spectrometer efficiency. While many earlier spectrometer designs rely on CsI-coated multi channel plate detectors (e.g.[1-5]), we use a back-illuminated charge coupled device (CCD) detector from Andor Technology PLC. Comparable detectors were used in the instruments described in [8,10,11,17,18,20]. This choice, together with the optimized detector geometry (normal incidence compared to grazing incidence for Rowland circle spectrometers) increases the overall spectrometer efficiency further. A drawback is the high detector sensitivity to visible light, which requires keeping the experiment dark during data acquisition. A set of baffles between grating and detector traps the visible light emitted from fluorescing samples.

We compared the overall efficiency of our spectrometer with the one permanently installed at beamline 8.0.1 of the ALS[3]. After adjusting its entrance slit to a comparable resolving power, the comparison revealed an approximate gain of two orders of magnitude for all four edges. As will be discussed in Section 4, this significant improvement allows us to collect more than

100 individual spectra within 10 to 30 minutes and to compile them in a two-dimensional RIXS map.

3.2 Resolving power

The selection of different diffraction orders for the different energies keeps the resolving power above 1000 over the whole spectral range despite the use of only one grating. Fig. 2 demonstrates how the resolving power is limited (by source size, aberration, or spatial resolution of the CCD detector) as a function of photon energy and selected order. For the energies of interest for our application, we find a resolving power of 1200 or higher at a source spot size as large as (30 × 3000) μm^2. In this case (and as shown in Fig. 2), the resolving power is exclusively limited by the source size. For lower source spot sizes, the physical resolution limit of the CCD becomes the limiting factor. It is about 25 microns [18].

Experiments performed at beamline 8.0.2 confirm these theoretical considerations. As refocusing optics two bendable mirrors were used, allowing spot sizes down to 15 x 100 microns[21]. The narrowest recorded elastically scattered peaks with an energy of 162 eV had a width of 2.5 CCD pixels full width at half maximum (FWHM), corresponding to a resolving power of 1300. In this case, the resolution was mainly limited by the spatial resolution of the CCD.

Such extremely narrow peaks consist of only 6 CCD pixels in dispersive direction, which leads to artifacts typical for undersampled data. In order to get rid of such effects, we have developed software that increases the number of effective pixels by using a "super-resolution" reconstruction technique, the basic idea of which is published in [20]. We will describe it in the following by applying it step-by-step to an extremely narrow Rayleigh line.

During read out of the CCD, in non-dispersive direction, 32 CCD pixels are merged in the read out register, thereby reducing the native CCD resolution of 2048 to 64 slices. This accelerates the read out process and decreases the read out noise considerably. For the "super-resolution" approach, the CCD is intentionally rotated by approx. 0.1 degree relative to the emission lines. The resulting image of an elastic peak (Rayleigh line) is shown in Fig. 4, expanded in the horizontal direction by a factor of 100. Each slice contains the same spectrum, but with a sub-pixel shift relative to its adjacent slices. This additional spatial information can be used to reconstruct a super-resolution spectrum. In our example, we increase the number of effective pixels by a factor 4. In order to achieve this, we first separate the total shift of each slice with respect to the center slice as calculated from the CCD rotation angle into a whole and a fractional pixel shift. The whole pixel shift is eliminated in each single-slice spectrum by appropriate counter-shifts (e.g. for a single-slice spectrum with a calculated pixel shift of 2.3 pixels, the intensity stored in pixel number *i* is shifted to pixel number *i*-2, leaving a residual sub-pixel shift of 0.3). The next step is to sort the resulting 64 sub-spectra by their sub-pixel shift into 4 bins. Bin 1 contains all spectra having a shift between 0 and 0.25 pixels, bin 2 from 0.25 to 0.5 pixels, and so forth. The sub-spectra in each bin are added up and divided by the number of contributing spectra, resulting in the 4 topmost spectra in Fig. 5 a) which have been shifted taking the sub-pixel shifts into account, as indicated by the black line at the left. These spectra are added up to the super-resolution spectrum (bottom spectrum in Fig. 5 a).

Applying this super-resolution procedure to a fictional δ-peak leads to the triangular response function shown as black bars in Fig 5 b). The FWHM of this narrowest possible peak is one CCD pixel (or 4 super-resolution pixels). This means that in order to resolve features which are narrower than one detector pixel, we would have to deconvolve the super-resolution

spectrum by this response function. A true deconvolution is impossible (and not necessary due to the spatial CCD resolution which is limited to 25 microns or approx. 2 pixels), since the Fourier transform of the response function contains zeros. Nevertheless, the spectra can be narrowed to some extent by applying the iterative van Cittert deconvolution method [22,23]. Fig. 5 b) shows the result of 3 van Cittert iterations (dashed line and squares) together with the original super-resolution spectrum (solid line and circles). Note that while the described super-resolution technique is very useful in order to avoid undersampling artifacts, deconvolution is not obligatory in our case, since the resolution is always limited by the source size and the spatial CCD resolution (see Fig. 2), not by the pixel size.

4. A RIXS map of HOPG

The high transmission of the new spectrometer allows to acquire and present resonant inelastic soft x-ray scattering data on an unprecedented level of detail. As will be discussed in this section, we can now collect complete "RIXS maps" instead of a series of spectra with selected excitation energies around the absorption edge. A RIXS map is a two-dimensional plot of the emission intensity as a function of both, emission and excitation energies. We have demonstrated the capabilities of this approach for the first time in [24] by investigating the oxygen K edge of liquids. We have also used this method for comparing a complete sulfur $L_{2,3}$ RIXS map of CdS with theoretical intensity maps in [25].

In this work, we present a carbon K RIXS map of highly oriented pyrolytic graphite (HOPG), which is shown in Fig. 6. The acquisition time for the whole map consisting of 60 individual RIXS spectra was 10 minutes (i.e. 10 seconds per spectrum). Each emission spectrum in the map has been individually normalized to the synchrotron intensity measured as photocurrent from a clean gold mesh placed between the last beamline mirror and the sample. Previous RIXS studies of HOPG are reported in [3,26-32]. With the exception of [26,32], the data in these studies was taken at the same beamline as our RIXS map (8.0.1, Advanced Light Source) using the permanently installed Rowland type spectrometer described in [3] and significantly longer acquisition times per spectrum. Symmetry-resolved x-ray emission studies of graphite are reported in [26,32]. Therein, the C K emission spectra were separated into contributions from σ and π bands by varying the detection angle.

Our RIXS data was taken in normal excitation geometry, with the emission detected 35° from the surface normal. Thus, π^*-excitation is inhibited. Indeed, we find a strong suppression of π-band emission, which results in a sharp intensity drop for emission energies above 280.5 eV (Fig. 6; note that this sharp drop is indeed a spectral feature and not, e.g., a normalization artifact). Furthermore, the most prominent changes in the emission spectra at the π^*-resonance (excitation energy: 285.5 eV) are suppressed as well, compared to [3,27-31]. Apart from these apparent differences, the data is in good agreement with published RIXS data. All dispersive features described in [3,27-31] on the basis of the Kramers-Heisenberg formalism[33-35] are present in our data. They are manifestations of the dispersion of both valence and conduction bands, as can be seen in Fig. 4 of [29].

In addition to the previously published interpretations we note the following findings which are based on the new insight derived from the RIXS maps and high quality data shown in Fig. 6. As mentioned above, the σ^* resonance (at an excitation energy of 291.5 eV) is enhanced in our experimental geometry. Some new insights in the resonant behavior of the emission spectra in the proximity of the σ^* resonance will be briefly discussed on the basis of the band structure of Fig. 3a in [30]. At an excitation energy of 292 eV, slightly above the σ^* resonance, the most prominent resonant emission feature located at an emission energy of 281.5 eV reaches its maximal resonantly enhanced intensity. Carlisle et al. report[29] that this feature

shows no visible dispersion and thus attribute it to an excitation into core-excitonic states at the M-point of the Brillouin zone. In contrast, our map clearly shows Raman dispersion parallel to the Rayleigh line below the σ^* threshold (excitation energies between 290 and 292 eV). Above 292 eV, it remains at its final position. The observed constant energy loss can be described as electronic Raman scattering, requiring occupied and unoccupied states with high density and an energy separation which is equal to the energy loss. The energy loss of 10 eV is in good agreement with the energy separation of the π- and σ^* bands at the M-point of the band structure reported in Fig. 3a in [30]. The fact, that in Fig. 6 of this work the intensity of this feature at its resonance (292.0 eV) dominates the π emission intensity, corroborates the assignment of E. L. Shirley[30] to π-σ^* interband transitions, since, in our case, σ^*-excitations are enhanced due to the experimental geometry. This transition may have a valence-excitonic final state.

Right at resonant excitation into the σ^* band at the M point (excitation energy of 292.0 eV), a weak and broad emission feature appears at an emission energy of 286.3 eV, together with a low-energy tail of the resonantly enhanced Rayleigh line, which extends down to an emission energy of 289.0 eV. While the enhancement of the Rayleigh line stems from radiant decay of the previously excited electron from the σ^* band at the M-point into the 1s orbital, we believe that the broad feature and the low-energy tail result from electron-phonon scattering processes during the core hole lifetime that neither conserve energy nor momentum. In these processes, the excited electron can be transferred from the σ^* band at the M-point towards the σ^* band minimum at the Γ-point (compare Fig. 3a in [30]), causing the low-energy tail of the Rayleigh line. The scattering process can also transfer the electron to the lower π^* bands between the M- and K-point, which leads to radiation around 286.3 eV upon its decay to the 1s level. This interpretation also explains the large width of these emission features, since the scattered electron can end up in any place of the Brillouin zone containing lower π^* and σ^* bands.

The good statistics of the RIXS map allows the extraction of emission spectra at any excitation energy, as well as partial fluorescence yield (PFY) absorption spectra at any emission energy inside the map. This is due to the fact that a RIXS map contains the full electronic information accessible by soft x-ray techniques. Compared to conventional RIXS studies with only a few resonant emission spectra at selected excitation energies, the 2D map is thus capable to make resonant effects much more apparent and comparatively easy to characterize. For example, the often crucial question whether a change in the emission spectra is due to intensity redistribution within several components or rather an energy shift of a single component can be answered with confidence.

The extraction of partial fluorescence yield spectra with deliberately selected emission energy detection window is described in literature as “selective XAS” [36], which allows to remove the core hole lifetime broadening in XAS spectra[37] if the resolution of the spectrometer is higher than the core hole lifetime broadening. Another possibility is to extract species- or site-selective XAS spectra if emission features are present which are indicative of a certain species or a special site. Finally, the intensities of different decay channels can be compared as a function of the excitation energy (decay channel-specific XAS[24]), yielding local information on the wave function overlap of the involved electronic states. Conventional soft x-ray spectrometers do not provide sufficient statistics at the high energy resolution required for both the synchrotron source and the spectrometer in order to extract such selective XA spectra, but with the here-described spectrometer and the RIXS map approach this can now be readily performed.

5. Summary

We describe the optical design and performance of a novel soft x-ray emission spectrometer, consisting of a spherical mirror, a blazed plane VLS grating, and a back-illuminated CCD detector in normal incidence geometry. It covers the photon energy range from 130 to 650 eV at a resolving power of >1200 with only one grating by making use of suitable diffraction orders. This approach also optimizes the detection efficiency. The optical design (including the variable line spacing parameters) was optimized by a novel analytical ray tracing algorithm. In order to increase the spatial detector resolution, we make use of a super-resolution reconstruction technique. Due to the two orders of magnitude higher detection efficiency compared to existing spectrometers it is possible to record complete two-dimensional RIXS maps in much less than one hour. As an example, the RIXS map of HOPG is shown and discussed. The map reveals details which allow assigning selected emission features to electron-phonon scattering and electronic Raman scattering, in addition to what has been published before.

6. Acknowledgment

We are grateful to the ALS and CXRO staff for technical support and in particular to Jim Underwood for helpful discussions. This work was supported by the German BMBF (project No. 05 KS4WWA/6), the DFG Emmy Noether program (M. Bär), and by the U.S. Department of Energy, Golden Field Office, through grant number DE-FG36-05GO85028. The ALS is supported by the Office of Basic Energy Sciences of the U.S. Department of Energy under Contract No. DE-AC02-05CH11231.

References:

[1] T. A. Callcott, K. L. Tsang, C. H. Zhang, D. L. Ederer, and E. T. Arakawa, Rev. Sci. Instrum. **57**, 2680 (1986).

[2] J. Nordgren, G. Bray, S. Cramm, and R. Nyholm, Rev. Sci. Instrum. **60**, 1690 (1989).

[3] J. J. Jia, T. A. Callcott, J. Yurkas, A. W. Ellis, F. J. Himpsel, M. G. Samant, J. Stöhr, D. L. Ederer, J. A. Carlisle, E. A. Hudson, L. J. Terminello, D. K. Shuh, and R. C. C. Perera, Rev. Sci. Instrum. **66**, 1394 (1995).

[4] J. Nordgren, J. Electron Spectrosc. Relat. Phenom. **110**, 1 (2000).

[5] S. Shin, A. Agui, M. Fujisawa, Y. Tezuka, T. Ishii, and N. Hirai, Rev. Sci. Instrum. **66**, 1584 (1995).

[6] H.A. Rowland, Philosophical Magazine **13**, 469 (1882).

[7] K. D. Osborn and T. A. Callcott, Rev. Sci. Instrum. **66**, 3131 (1995).

[8] C. F. Hague, J. H. Underwood, A. Avila, R. Delaunay, H. Ringuenet, M. Marsi, and M. Sacchi, Rev. Sci. Instrum. **76**, 023110 (2005).

[9] C. Dallera, E. Puppin, G. Trezzi, N. Incorvaia, A. Fasana, L. Braicovich, N. B. Brookes, and J. B. Goedkoop, J. of Synchrotron Radiation, **3**, 231 (1996).

[10] D. Cocco, M. Zangrando, M. Matteucci, F. Bondino, M. Platè, M. Zacchigna, F. Parmigiani, B. Nelles, and K.C. Prince, AIP Conf. Proc. **705**, 873 (2004).

[11] T. Tokushima, Y. Harada, H. Ohashi, Y. Senba, and S. Shin, Rev. Sci. Instrum. **77**, 063107 (2006).

[12] M. C. Hettrick and J. H. Underwood, Appl. Optics, **25** (1986) 4228.

[13] M. C. Hettrick, J. H. Underwood, P. J. Batson and M. J. Eckart, Appl. Optics, **27** (1988) 200.

[14] M. C. Hettrick and J. H. Underwood, AIP Conf. Proc. **147**, 237 (1986).

[15] M. C. Hettrick and J. H. Underwood, U.S. Patent No. 4,776,696 (Oct. 11, 1988).

[16] J. H. Underwood, Z. Hussain, W. R. McKinney, and T. Warwick, Light Source Note LSBL-622.

[17] Y. Chuang, J. Pepper, W. McKinney, Z. Hussain, E. Gullikson, P. Batson, D. Qian, M. Z. Hasan, Journal of Physics and Chemistry of Solids **66**, 2173 (2005).

[18] G. Ghiringhelli, A. Piazzalunga, C. Dallera, G. Trezzi, L. Braicovich, T. Schmitt, V.N. Strocov, R. Betemps, L. Patthey, X. Wang, and M. Grioni, Rev. Sci. Instrum. **77** (2006) 113108.

[19] O. Fuchs, L. Weinhardt, C. Heske, E. Umbach, R. Follath, Y.D. Chuang, W.R. McKinney, and Z. Hussain, Light Source Note LSBL-875.

[20] H. Tsunemi, S. Nomoto, K. Hayashida, E. Miyata, H. Murakami, Y. Kato, G. Yuan, K. Murai, R. Kodama, and H. Daido, Appl. Phys. B, **57**, 331 (1993).

[21] J. D. Denlinger, ALS Activity Report 2006, 116 (2007).

[22] P. H. van Cittert, Z. Phys. A, **69**, 298 (1932).

[23] H. C. Burger and P. H. van Cittert, Z. Phys. A, **79**, 722 (1932).

[24] L. Weinhardt, O. Fuchs, M. Blum, M. Bär, M. Weigand, J.D. Denlinger, Y. Zubavichus, M. Zharnikov, M. Grunze, C. Heske, and E. Umbach, in print.

[25] L. Weinhardt, O. Fuchs, A. Fleszar, M. Bär, M. Blum, M. Weigand, J.D. Denlinger, W. Yang, W. Hanke, E. Umbach, and C. Heske, Phys. Rev. B **79**, 165305 (2009).

[26] P. Skytt, P. Glans, D. C. Mancini, J. H. Guo, N. Wassdahl, J. Nordgren and Y. Ma, Phys. Rev. B **50**, 10457 (1994).

[27] J. A. Carlisle, Eric L. Shirley, E. A. Hudson, L. J. Terminello, T. A. Callcott, J. J. Jia, D. L. Ederer, R. C. C. Perera, and F. J. Himpsel, Phys. Rev. Lett. **74**, 1234 (1995).

[28] J. A. Carlisle, E. L. Shirley, L. J. Terminello, J. J. Jia, T. A. Callcott, D. L. Ederer, R. C. C. Perera, and F. J. Himpsel, Phys. Rev. B **59**, 7433 (1999).

[29] J. A. Carlisle, S. R. Blankenship, L. J. Terminello, J. J. Jia, T. A. Callcott, D. L. Ederer, R. C. C. Perera, and F. J. Himpsel, J. Electron Spectrosc. Relat. Phenom. **110** 323 (2000).

[30] E. L. Shirley, J. Electron Spectrosc. Relat. Phenom. **110** (2000) 305.

[31] A. V. Sokolov, E. Z. Kurmaev, S. Leitch, A. Moewes, J. Kortus, L. D. Finkelstein, N. A. Skorikov, C. Xiao, and A. Hirose, Journal of Physics: Condensed Matter, **15**, 2081 (2003).

[32] J. Guo, P. Skytt, N. Wassdahl, and J. Nordgren, J. Electron Spectrosc. Relat. Phenom. **110**, 41 (2000).

[33] H. Kramers and W. Heisenberg, Z. Phys. **31**, 681 (1925).

[34] V. Weisskopf and E. Wigner, Z. Phys. **63**, 54 (1930).

[35] Y. Ma, Phys. Rev. Lett. **69**, 2598 (1992).

[36] F. de Groot, Chem. Rev. **101**, 1779 (2000).

[37] K. Hämäläinen, D.P. Siddons, J.B. Hastings, and L.E. Berman, Phys. Rev. Lett. **67**, 2850 (1991).

[38] Andor Technologies PLC, operating manual for CCD model DO436

Figure captions:

Figure 1: Sketch of the optical path of the soft x-ray spectrometer with source S. The aperture A can be used to mask the spherical mirror M. G denotes a blazed VLS grating, and D a back-illuminated CCD detector in normal incidence geometry.
Figure 2: The different limitations (see inset) of the resolving power as a function of photon energy and diffraction order. For calculating the aberration limit, a fully illuminated mirror (i.e. with open aperture A) was assumed.

Figure 3: Comparison of the measured (squares) and calculated (triangles) grating efficiencies for the four photon energies of interest in their respective diffraction orders. The efficiencies were measured at beamline 6.3.2. For the calculations a micro-roughness of 10 Å was assumed.

Figure 4: The narrow Rayleigh line as it appears on the rotated CCD detector, allowing the use of the super-resolution technique. The image is binned to 64 slices in the vertical direction and expanded by a factor of 100 in the horizontal direction.

Figure 5: a) The 4 top spectra (dashed) show the sums of 4 groups of slices selected and shifted by their sub-pixel shifts. The bottom spectrum is the sum of the 4 spectra above. b) The solid line with circles is a copy of the lowest spectrum in a), the black bars represent the response function of the super-resolution technique to a δ-function, and the dashed line with rectangles shows the spectrum deconvolved by the response function using 3 van Cittert iterations.

Figure 6: Resonant inelastic soft x-ray scattering (RIXS) map of HOPG. The arrows denote areas of the map with predominant σ- and π-emission, as well as σ^*- and π^*-excitation. The Fermi level E_F is marked on both axes.

Table 1:

Design Specs:	Angles (see Fig. 1)	α=87.9°	β=84.1°	φ=172°	
	Distances (see Fig. 1)	r_1=400 mm	r_2=100 mm	r_3=1000 mm	
Mirror Specs:	Dimensions	(20 × 80) mm^2			
	Radius of Curvature	8410 mm			
Grating Specs:	Dimensions	(20 × 110) mm^2			
	Blaze angle	1.79° for inner (positive) orders			
	Central groove density	a_0 = 600 lines/mm			
	VLS parameters	a_1 = 1.19634 lines/mm^2			
		a_2 = 1.27512*10^{-3} lines/mm^3			
		a_3 = 1.11401*10^{-6} lines/mm^4			
	Rule density [lines/mm]	$n(x) = a_0 + a_1 x^1 + a_2 x^2 + a_3 x^3$			
Detector Specs:	Dimensions	(27.6 × 27.6) mm^2			
	Pixel dimensions	(13.5 × 13.5) μm^2			
Throughput:	Acceptance angle	(11.2 × 18.0) $mrad^2$			
	Emission line	S $L_{2,3}$	C K	N K	O K
	Emission energy (eV)	150	280	400	525
	Diffraction order	+1	+2	+3	+3
	Calc. mirror reflectivity	68 %	67 %	65 %	60 %
	Calc. grating efficiency	25 %	22 %	19 %	19 %
	Measured grating effi.	26 %	23 %	17 %	13 %
	Detector efficiency[34]	30 %	40 %	50 %	60 %
	Total detection efficiency	5.3 %	6.2 %	5.2 %	4.7 %

Table caption:

Table 1: Optical parameters as well as calculated reflectivities and efficiencies for the selected photon energies and diffraction orders. The total detection efficiency is calculated as the product of calculated mirror reflectivity, measured grating efficiency, and detector efficiency taken from the operating manual of the detector[34].

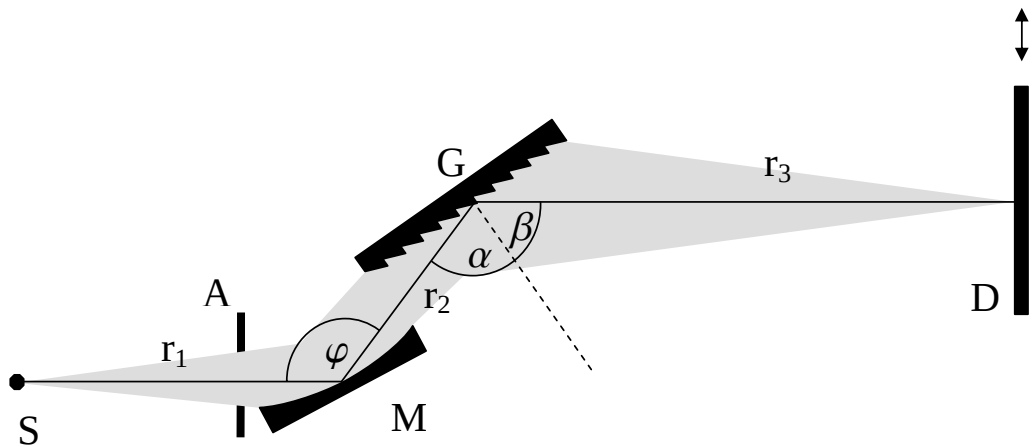
G
r3
β
α
A
r2
D
r1
φ
S
M

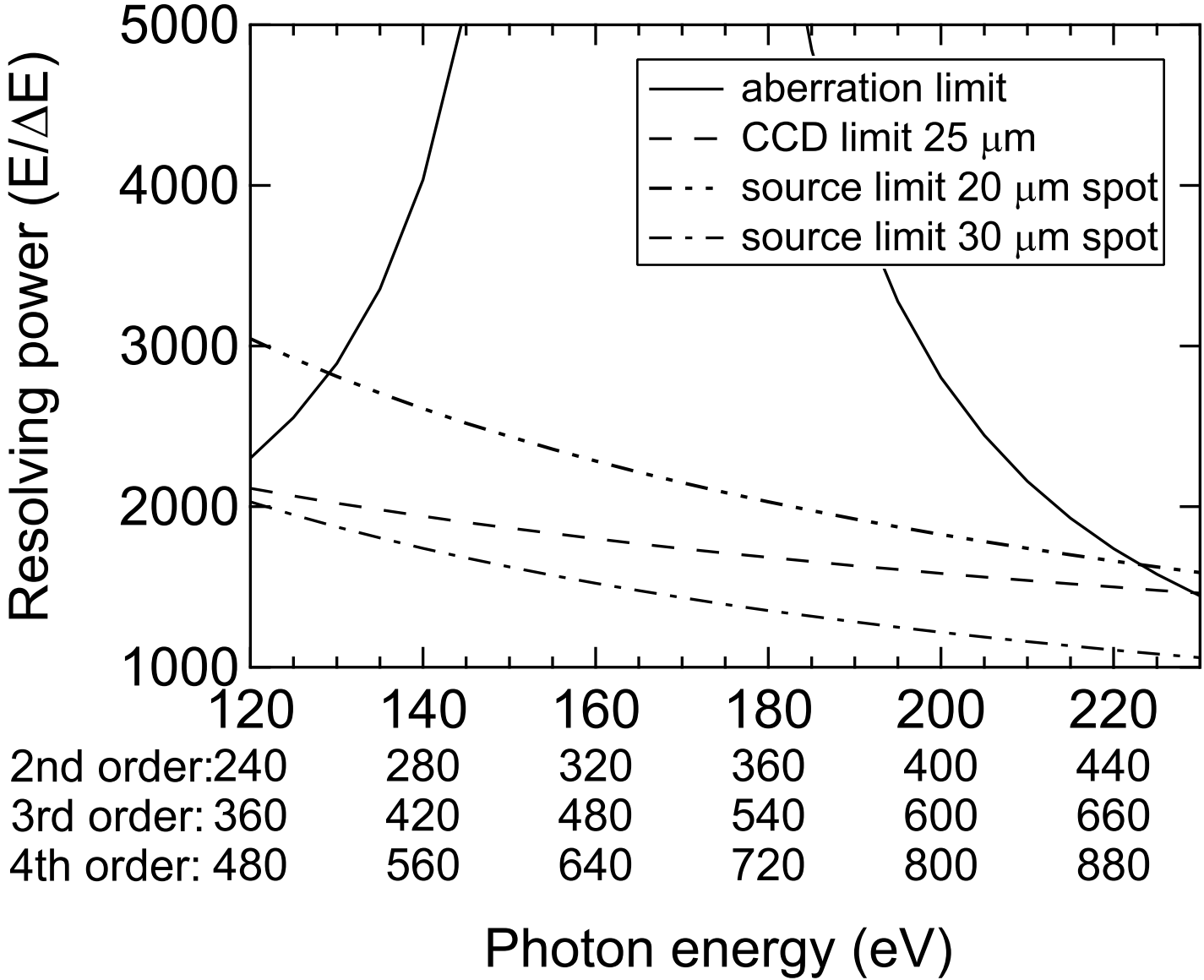
Resolving power (E/ΔE)
5000
4000
3000
2000
1000
aberration limit
CCD limit 25 μm
source limit 20 μm spot
source limit 30 μm spot
120
140
160
180
200
220
2nd order:240
280
320
360
400
440
3rd order: 360
420
480
540
600
660
4th order: 480
560
640
720
800
880
Photon energy (eV)

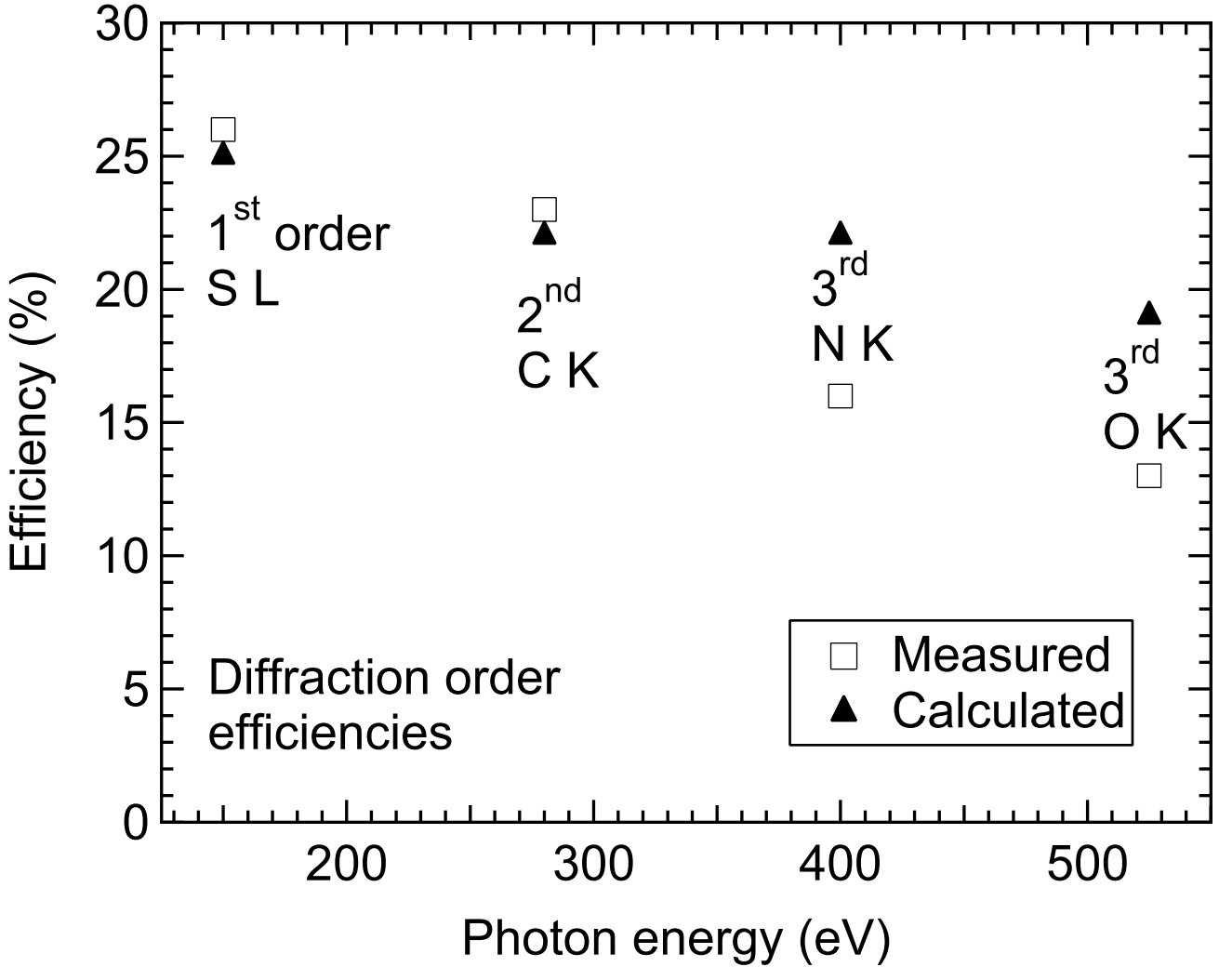
30
25
20
15
10
5
0
Efficiency (%)
200
300
400
500
Photon energy (eV)
1st order
S L
2nd
C K
3rd
N K
3rd
O K
Diffraction order
efficiencies
Measured
Calculated

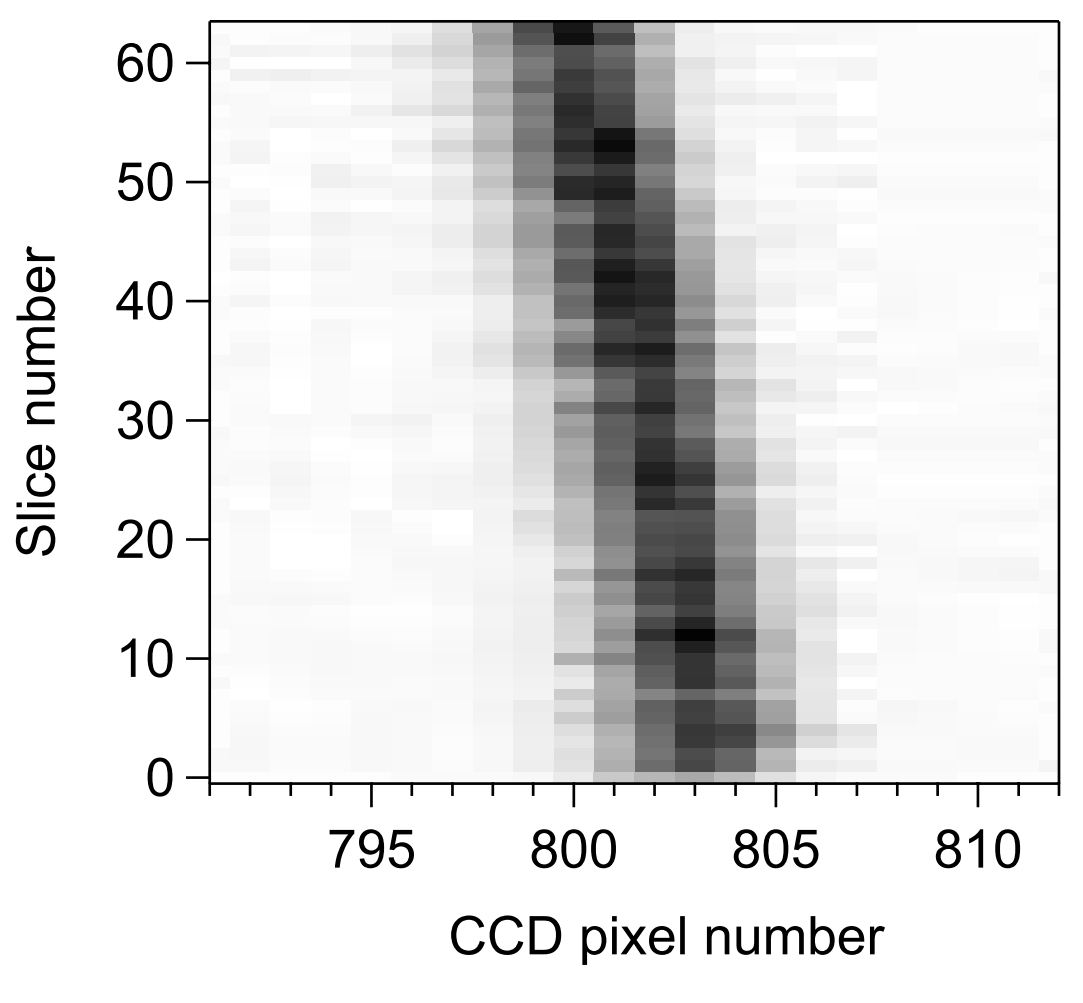
Slice number
60
50
40
30
20
10
0
795
800
805
810
CCD pixel number

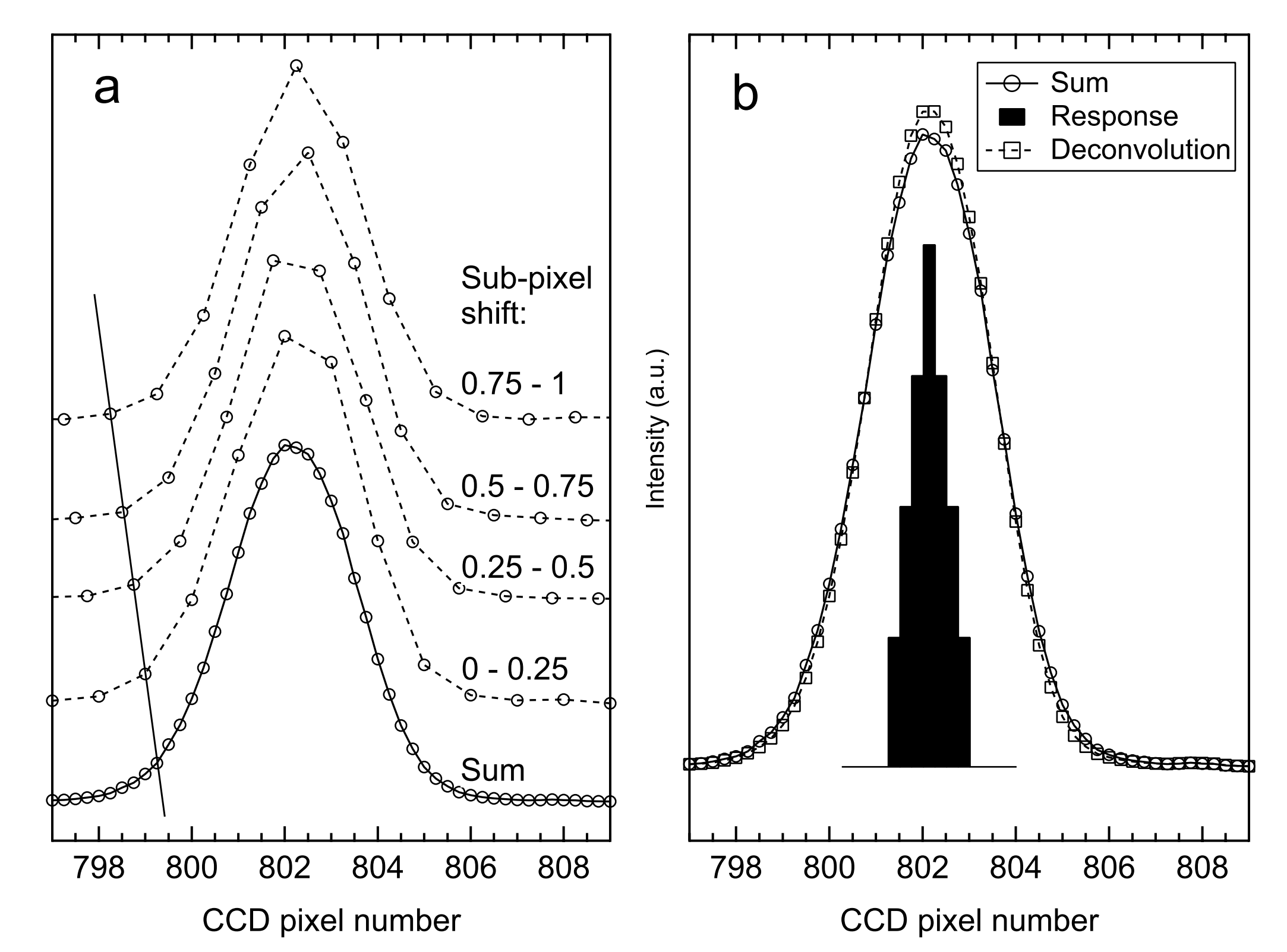
a
Sub-pixel shift:
0.75 - 1
0.5 - 0.75
0.25 - 0.5
0 - 0.25
Sum
798
800
802
804
806
808
CCD pixel number
b
Sum
Response
Deconvolution
Intensity (a.u.)
798
800
802
804
806
808
CCD pixel number

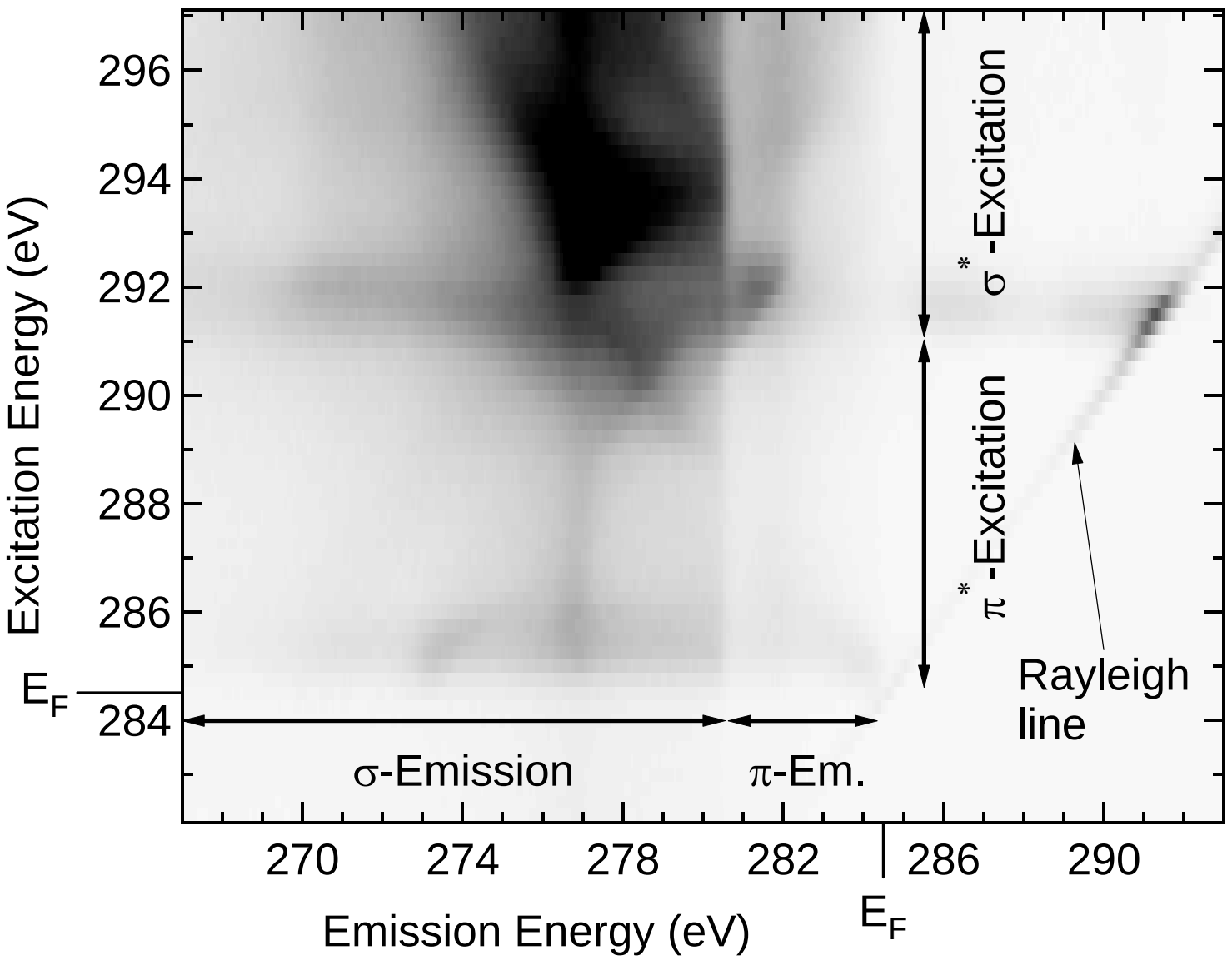
296
294
292
290
288
286
284
E_F
Excitation Energy (eV)
σ^*-Excitation
π^*-Excitation
Rayleigh line
σ-Emission
π-Em.
270
274
278
282
286
290
E_F
Emission Energy (eV)